High-speed Label-free Functional Photoacoustic Microscopy of Mouse Brain in Action

Junjie Yao[1], Lidai Wang[1], Joon-Mo Yang[1], Konstantin I. Maslov[1], Terence T. W. Wong[1], Lei Li[1], Chih-Hsien Huang[2], Jun Zou[2], Lihong V. Wang[1]

[1]*Optical Imaging Laboratory, Department of Biomedical Engineering, Washington University in St. Louis, St. Louis, MO, USA*

[2]*Department of Electrical and Computer Engineering, Texas A&M University, College Station, TX, USA*

Correspondence should be addressed to L.V.W. (lhwang@wustl.edu)

Supplementary Note 1. Water-immersible MEMS scanning mirror

A schematic of the customized MEMS scanning mirror is shown in Figures S1b–c. The elliptical MEMS mirror plate (thickness: 0.5 mm) is made of a 100-μm-thick silicon wafer with an 80-nm-thick enhanced aluminum coating, and provides good reflection of both the optical beams (optical reflectivity: ~98%) and acoustic beam (acoustic reflectivity: ~100%). The mirror plate, 9 mm long and 6 mm wide, is supported by two 1.0×0.9 mm^2 hinges made of high-strength flexible polymer, which can resist surface tension forces in liquids. To actuate the mirror plate, highly efficient electromagnetic force is generated by a compact inductor coil (inductance: 33 mH) and a pair of high-strength rare-earth permanent magnets (diameter: 3.1 mm) on the back of the mirror plate. A sinusoidal current applied to the inductor coil generates a magnetic field with alternating polarity and strength, which drives the mirror plate to oscillate around the hinges. By controlling the frequency and amplitude of the driving current, the scanning speed and range of the mirror plate can be adjusted accordingly.

Several critical changes have been made to the previously reported prototype MEMS mirror [1]. (1) The metal coating on the mirror surface has been changed from gold to aluminum. Although gold is chemically more inert in a water environment, the 50% reflectivity of the gold coating at 532 nm results in significant heating of the mirror surface, and accelerates mirror fatigue when repeated volumetric imaging is performed. The aluminum coating has enhanced the optical reflectivity to more than 98%, dramatically reducing the excitation fluence loss and slowing

down fatigue. (2) The thickness of the silicon wafer of the mirror plate has now been reduced from 500 μm to 100 μm. The thinner silicon wafer reduces the mass of the mirror plate and thus the required driving force, extending the supporting hinges' lifetime. (3) The mirror plate has now been changed from a rectangle to an ellipse. The elliptic shape can better fit the acoustic spot and reduce the total plate mass. The damping force at the corners of the mirror plate is dramatically reduced, and the scanning stability is significantly improved.

Supplementary Note 2. Simulation of photoacoustic signals with different excitation pulse widths

The photoacoustic effect converts optical energy to acoustic energy. The conversion efficiency is related to the temporal profile of optical energy deposition (i.e., temporal profile of the excitation pulse). A short pulse is usually used to generate wideband photoacoustic signals. Note that a time-invariant light beam (with constant output intensity) cannot generate photoacoustic signals. In our oxygen saturation (sO_2) measurement, two lasers with different pulse widths are used. Below, PA signals that are produced below the saturation intensity and observed at the source and detector are numerically simulated.

Matching the lateral resolution of our system, a 3-µm-diameter microsphere is used as the target. Two Gaussian-profile laser pulses with the same pulse energy but different pulse widths (3 ps and 3 ns) are used as the excitation sources. As shown in **Supplementary Fig. 2a**, PA signal generated by the picosecond excitation has a greater peak-to-peak amplitude than that by the nanosecond excitation when observed at the target before acoustic propagation. Frequency analysis in **Supplementary Fig. 2b** shows that the difference of the two PA signals mostly falls into the frequency range higher than 70 MHz. In the frequency region lower than 70 MHz, the two PA signals are largely identical.

The high-frequency signals are quickly attenuated during propagation (acoustic attenuation in the brain: 0.8 dB/cm/MHz [2]) , and the remaining signals are captured by an ultrasonic transducer with a matched bandwidth. The final PA signals detected by the 50-MHz transducer used in our PAM system have virtually no difference under the two excitations (**Supplementary Fig. 2c**).

The above simulation is performed in linear situation where the excitation intensity is lower than the saturation intensity. When the pulse energy increases, the picosecond excitation induces more significant saturation than the nanosecond excitation due to its much greater intensity. This saturation difference forms the basis of the new pulse-width-based method for sO_2 measurement (see Online Methods for more details).

Supplementary Note 3. Effect of skull on imaging performance of PAM

Skull removal or thinning is commonly performed in optical microscopy of the mouse brain [3]. Imaging techniques that allow an intact skull are of interest for studies that require normal physiological conditions in the living brain. For example, the inflammatory reactions induced by skull removal have led to contradictory views on the degree of structural synaptic plasticity in the adult brain and how long-term information might be stored in synaptic circuits [3]. With PAM, there is no need to remove or thin the skull. However, the skull can potentially degrade PAM image quality in two ways. First, the skull blurs the optical focus. The blurring effect was investigated by CCD imaging of the optical focal spot beneath a mouse skull (Figures S6a–c). With a thickness of ~150 μm, the skull attenuated the laser fluence by ~10%, and blurred the focal spot by 8%. Second, the skull attenuates acoustic signals. By imaging a piece of uniform absorber partially covered by a mouse skull, we found that the skull attenuated the acoustic amplitude by 75% (Figures S6d–e). Due to the high signal-to-noise ratio in PAM, such signal attenuation is tolerable. To further study the effect of an intact skull on the imaging performance *in vivo*, we imaged a 2×2 mm^2 region of a mouse brain with and without the skull and dura (**Supplementary Fig. 7**). After removing the skull and dura, the average PA signal amplitude increased by ~200%, and the spatial resolution was improved with more capillaries imaged. We also noticed that after the skull and dura removal, some blood vessels vanished from the PAM image. The absent vessels were in the dura as evinced by their depths and signal amplitudes.

References

1. Huang, C.-H., Yao, J., Wang, L. & Zou, J. *Microsystem Technologies*, 1-6 (2012).
2. Azhari, H. Basics of biomedical ultrasound for engineers. (Wiley : IEEE, Hoboken (N.J.); 2010).
3. Yang, G., Pan, F., Parkhurst, C.N., Grutzendler, J. & Gan, W.B. *Nat Protoc* **5**, 201-208 (2010).

Supplementary tables, figures and videos

**Supplementary Table 1. Summary of PAM parameters for mouse brain imaging.**

Parameters		Fig. Fig.1d Wide-field morphology	Fig. 1e Depth-scanning	Fig. 1f Wide-field oxygenation	Fig. 2a Stimulation: perfusion	Fig. 2c Stimulation: oxygenation
Field of view (mm^2)		5.0 × 10.0	0.6 × 0.6	5.0 × 10.0	3.0 × 4.0	2.0 × 3.0
x step size (MEMS, μm)		2.5	2.5	4	2.5	8
y step size (motor, μm)		5	2.5	5	10	7.5
x scanning range (mm)		3	0.6	1.0	3	2
1D rate (kHz)	**ps**	500	100	100	500	100
	ns	NA	NA	100	NA	100
2D rate (Hz)		400	400	400	400	400
3D rate (Hz)		1/15[a]	0.2 (Depth-scan)[b]	1/40[c]	1	1
Pulse energy[d] (nJ)	**ps**	200	200	400	200	400
	ns	NA	NA	400	NA	400
Depth-scanning step size (μm)		NA	100	NA	NA	NA

[a] The 3D image was assembled by stitching three subregions of 3.0 × 10.0 mm^2.

[b] The depth-scan image was assembled by stitching 12 depth-scans with a step size of 100 μm.

[c] The 3D image was assembled by stitching eight subregions of 1.0 × 10.0 mm^2.

[d] The pulse energy was measured on the skull surface.
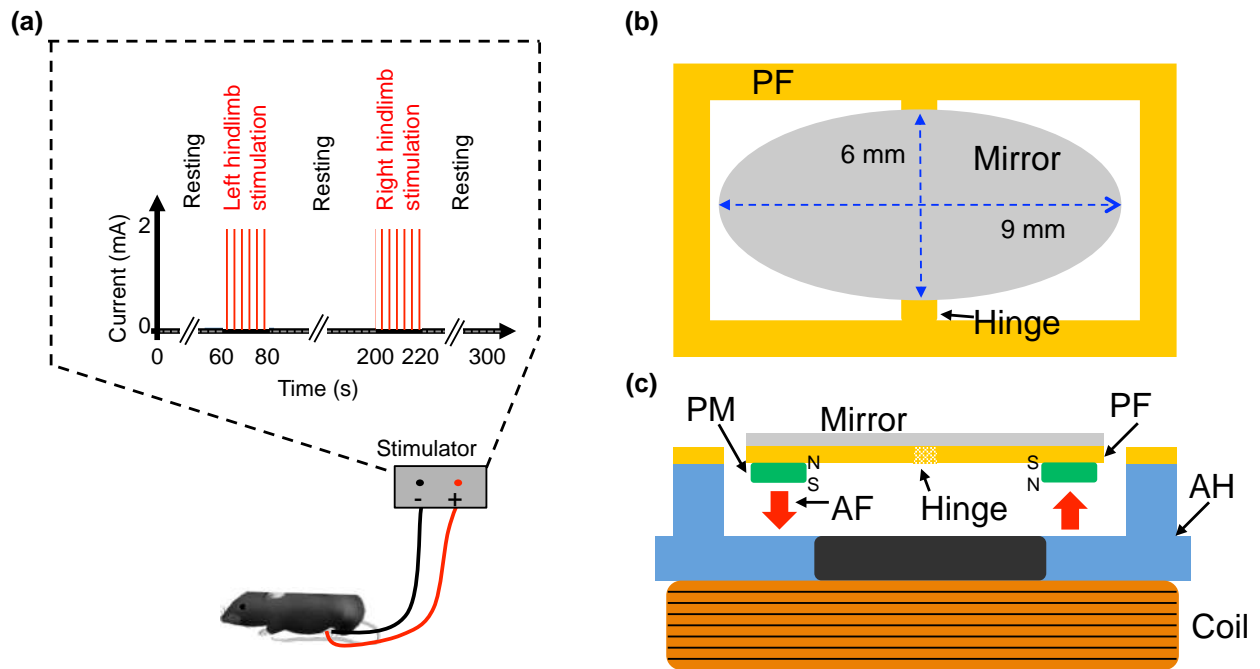
Supplementary Fig. 1. Sequence of electrical stimulations and schematic of MEMS mirror in PAM. (a) Time course of the electrical stimulations to the mouse hindlimbs, consisting of three resting periods and two stimulation periods. Each stimulation period consisted of a train of electrical pulses with an amplitude of 2 mA, a pulse width of 0.25 ms and a repetition rate of 2 Hz. (b) Top view of the water-immersible MEMS scanning mirror, showing the elliptical mirror plate and the supporting hinges. PF, polymer frame. (c) Side view of the mirror, showing the mirror plate driven by the actuation force generated by two permanent magnets and an inductor coil. AF, actuation force; AH, acrylic holder; PM, permanent magnet.
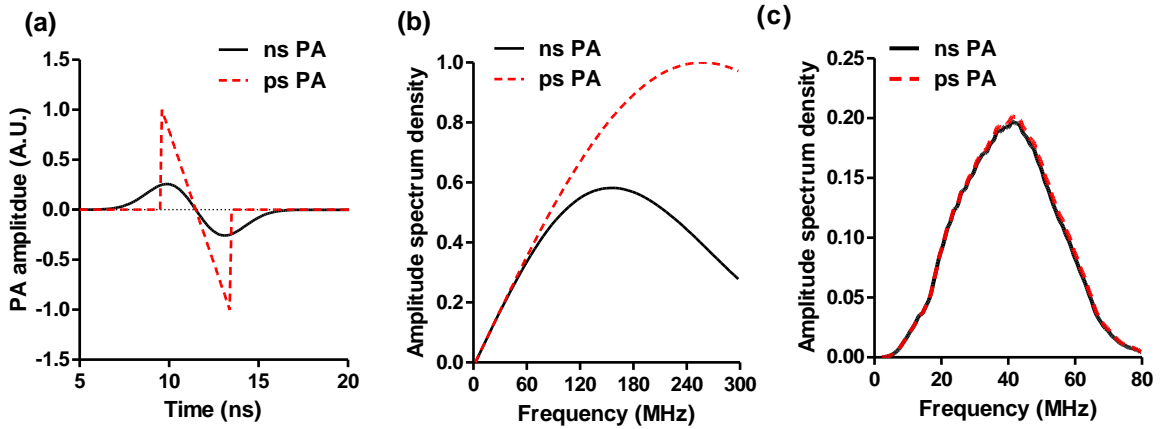
Supplementary Fig. 2. Simulation of PA signal generation and detection in PAM with different excitation pulse widths. (a) Generated PA signal profiles from a 3-µm-diameter sphere excited by a 3-ns pulse (ns PA) and a 3-ps pulse (ps PA) with the same pulse energy. (b) Frequency spectra of the generated PA signals. The picosecond excitation is more efficient in generating high frequency signals (>70 MHz). (c) Frequency spectra of detected PA signals by the ultrasonic transducer. The PA signals are attenuated during propagation. The PA signals generated with the two excitation pulse widths are nearly identical at the detector after propagating ~1 mm in brain tissue (acoustic attenuation: 0.8 dB/cm/MHz) and ~6 mm in water (acoustic attenuation: 0.002 dB/cm/MHz).
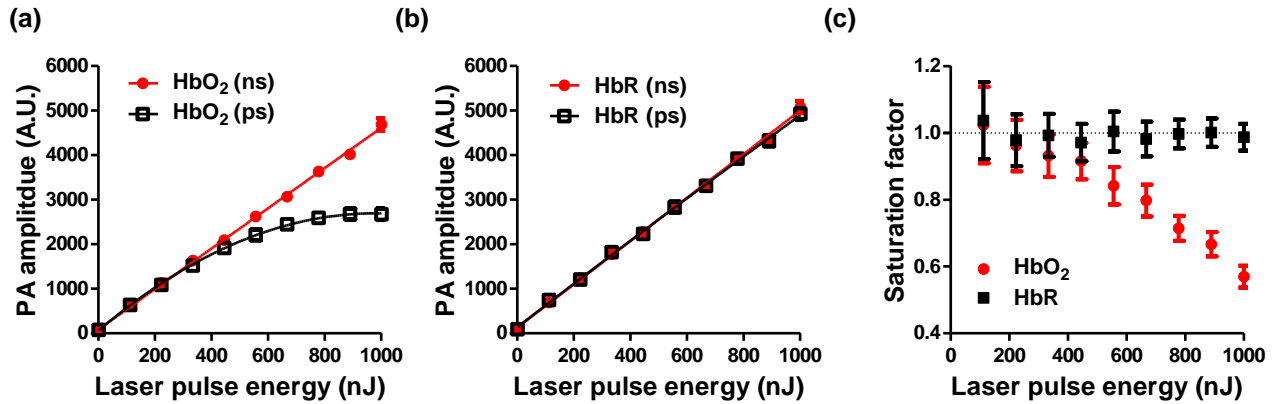
Supplementary Fig. 3. Absorption saturation of oxy- and deoxy-hemoglobin (HbO$_2$ and HbR). (a–b) PA amplitudes of HbO$_2$ (a) and HbR (b), as a function of excitation pulse energy with 3-ps and 3-ns pulse widths. To mimic the *in vivo* studies, the laser beam was focused at ~250 μm beneath the blood surface of a 300-μm-diameter tube filled with whole bovine blood. Note that the light can only penetrate ~40 μm into the blood. The laser spot size on the sample surface was ~50 μm. The results show that HbO$_2$ can be saturated more with picosecond excitation. (c) Saturation factors of HbO$_2$ and HbR. The saturation factor is defined as the ratio of the PA amplitude with picosecond excitation to that with nanosecond excitation.
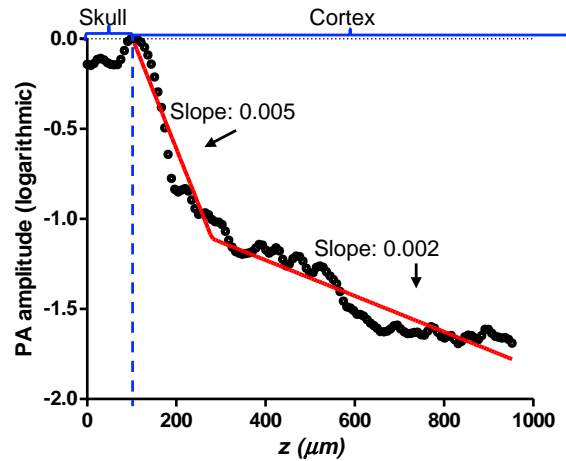
Supplementary Fig. 4. The average PA amplitude decay with the increasing depth, in natural logarithmic scale. The PA amplitude at a particular depth was represented by the average value of the brightest 0.1% of the pixels from that depth. From the exponential fit to the data, we were able to determine the characteristic attenuation length (CAL), which corresponds to a 1/e fold decay in the PA amplitude. A fast decay component with a CAL of ~200 μm was contributed by the signals from the optical resolution volume, so called Class I signals, and a slow decay component with a CAL of ~500 μm was contributed by the signals from the portion of the acoustic resolution volume that lies outside the optical resolution volume, so called Class II signals. The optical resolution volume in PAM is defined by the cylinder whose base is the optical focal spot and whose height is the acoustic axial resolution. Similarly, the acoustic resolution volume in PAM is defined by the cylinder whose base is the acoustic focal spot and whose height is the acoustic axial resolution.
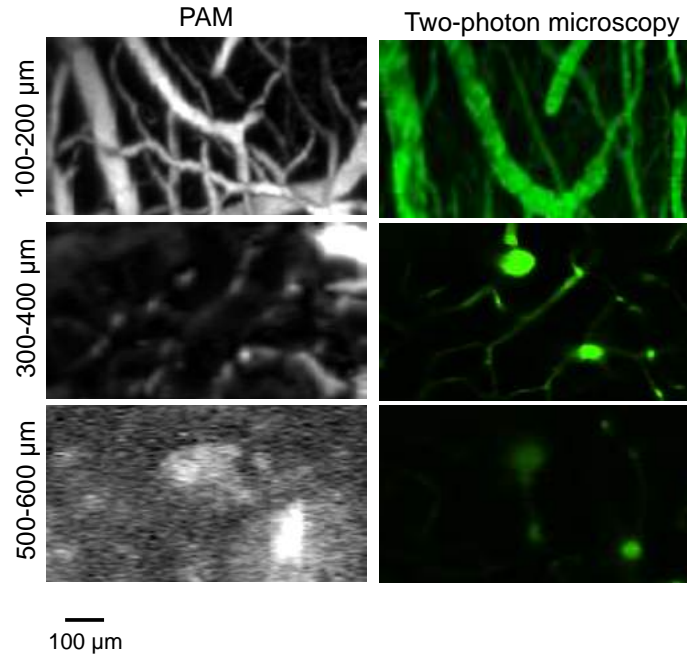
Supplementary Fig. 5. Comparison of the brain vasculature imaged by two-photon microscopy and PAM. The same mouse was first imaged by PAM, using hemoglobin as the endogenous contrast (left column), and then imaged by two-photon microscopy, using FITC-dextran as the exogenous contrast (right column). Three representative 100-µm-thick layers are shown. Each image was normalized by its own maximum intensity. The results show that PAM and two-photon microscopy have comparable image quality for the pia vessels (<200 µm deep). However, PAM cannot resolve the deep capillary beds as well as two-photon microscopy due to the use of a short wavelength for photoacoustic generation.
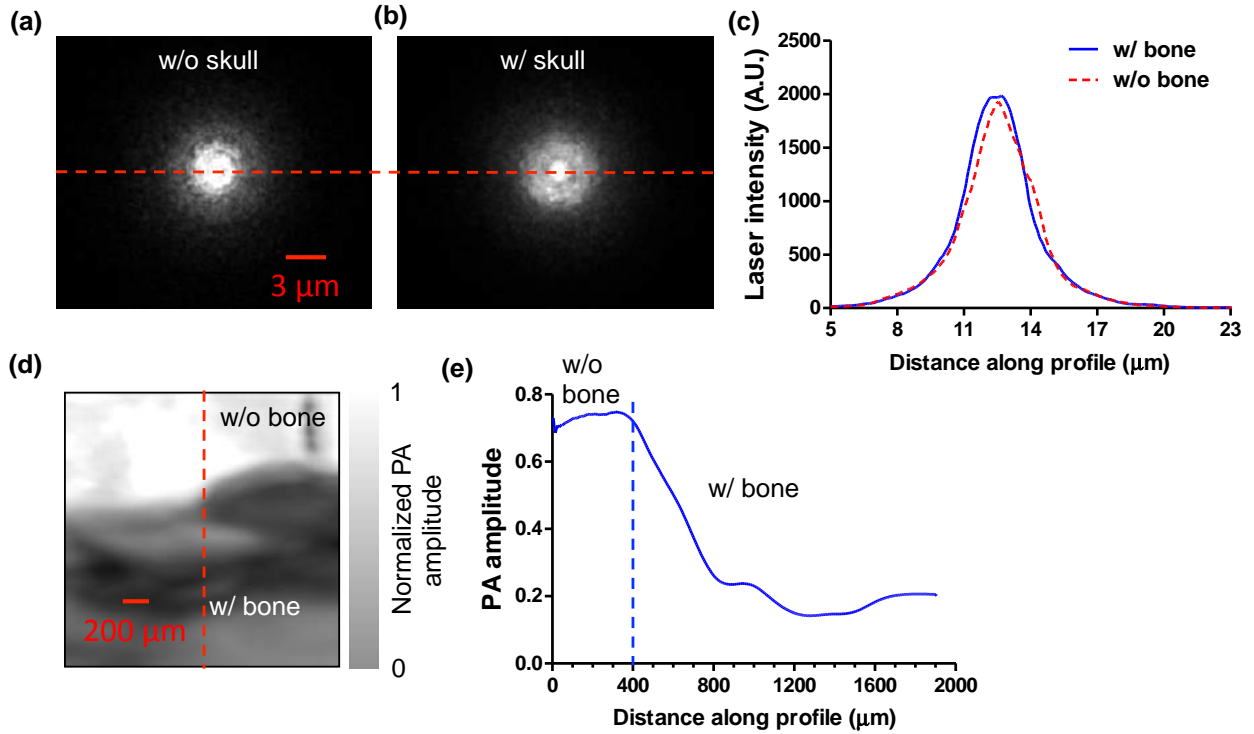
Supplementary Fig. 6. **Effect of mouse skull on the optical focusing and acoustic transmission in PAM.** (a) A CCD image of the optical focus in water, showing a focal spot size of ~3 µm. (b) A CCD image of the optical focus with the laser beam passing through a piece of mouse skull. (c) Light intensity profiles along the dashed lines in (a) and (b), showing that the skull induced marginal degradation in optical focusing. (d) A PAM image of a piece of black tape partially covered by a piece of mouse skull. (e) PA signal profile along the dashed line in (d), showing the signal attenuation by the skull.
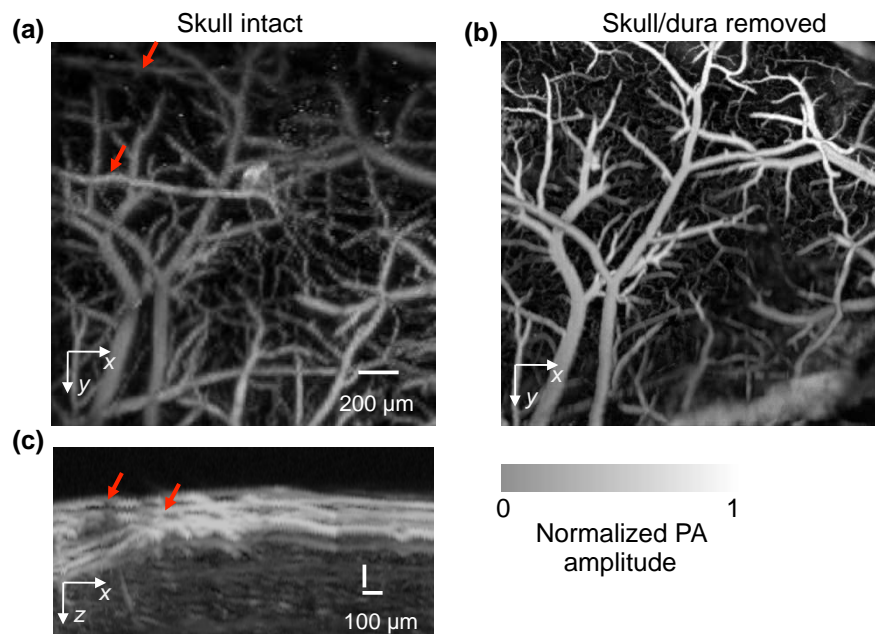
Supplementary Fig. 7. PAM of a mouse brain with and without the skull and dura. (a–b) *En face* PAM images of a 2×2 mm^2 region in a mouse brain acquired with the skull intact (a), and the skull and dura removed (b). With the skull and dura removal, large vessels were imaged with greater signal-to-noise ratios, more deep capillaries were imaged, but the spatial resolution was only marginally improved. Some vessels in (a), indicated by the arrows, were absent in (b). (c) An *x-z* projection of (a), showing that the absent vessels were from the surface of the brain.
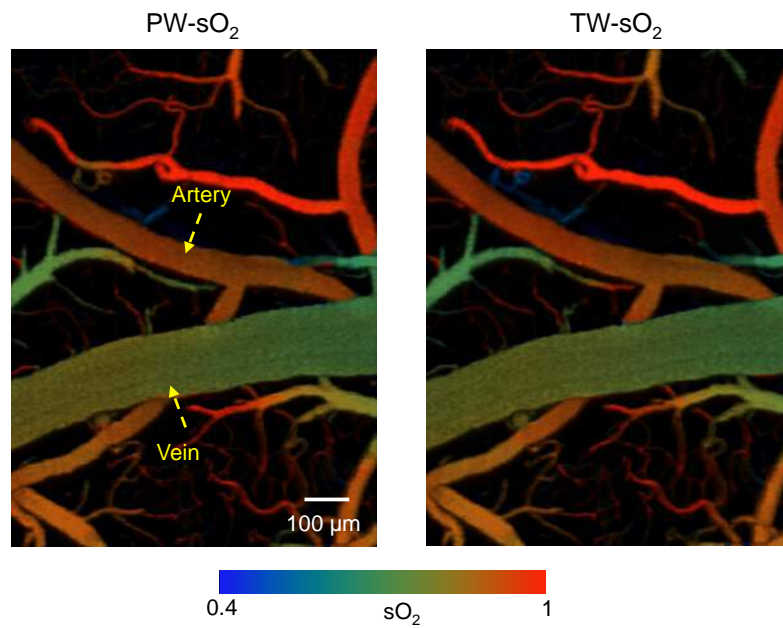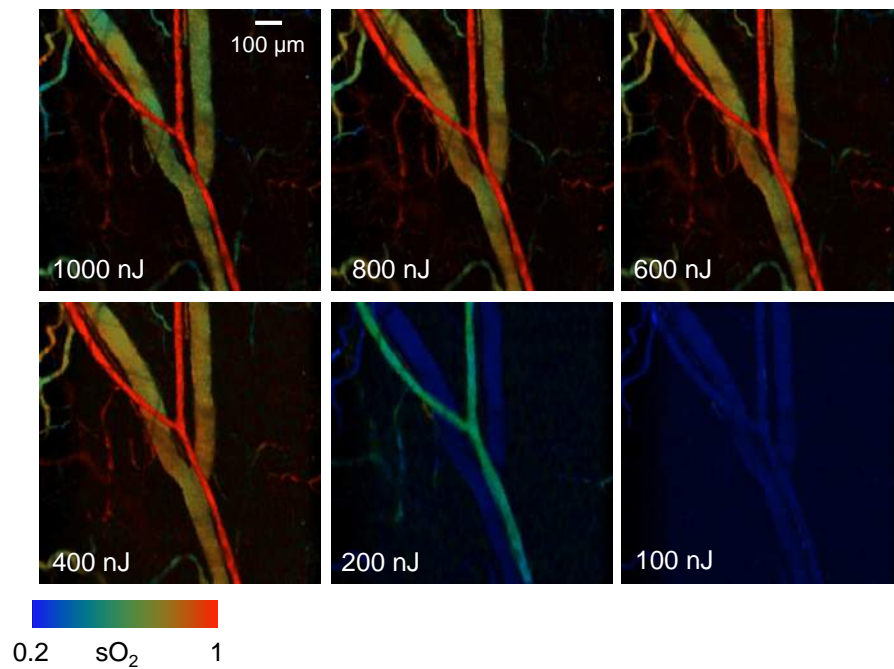
Supplementary Fig. 8. Comparative sO$_2$ measurements in a major cortical artery-vein pair, by using the pulse-width-based method (PW-sO$_2$) and two-wavelength-based method (TW-sO$_2$). The TW-sO$_2$ measurement was performed at 570 nm and 578 nm on a slow PA system with a wavelength tunable laser.
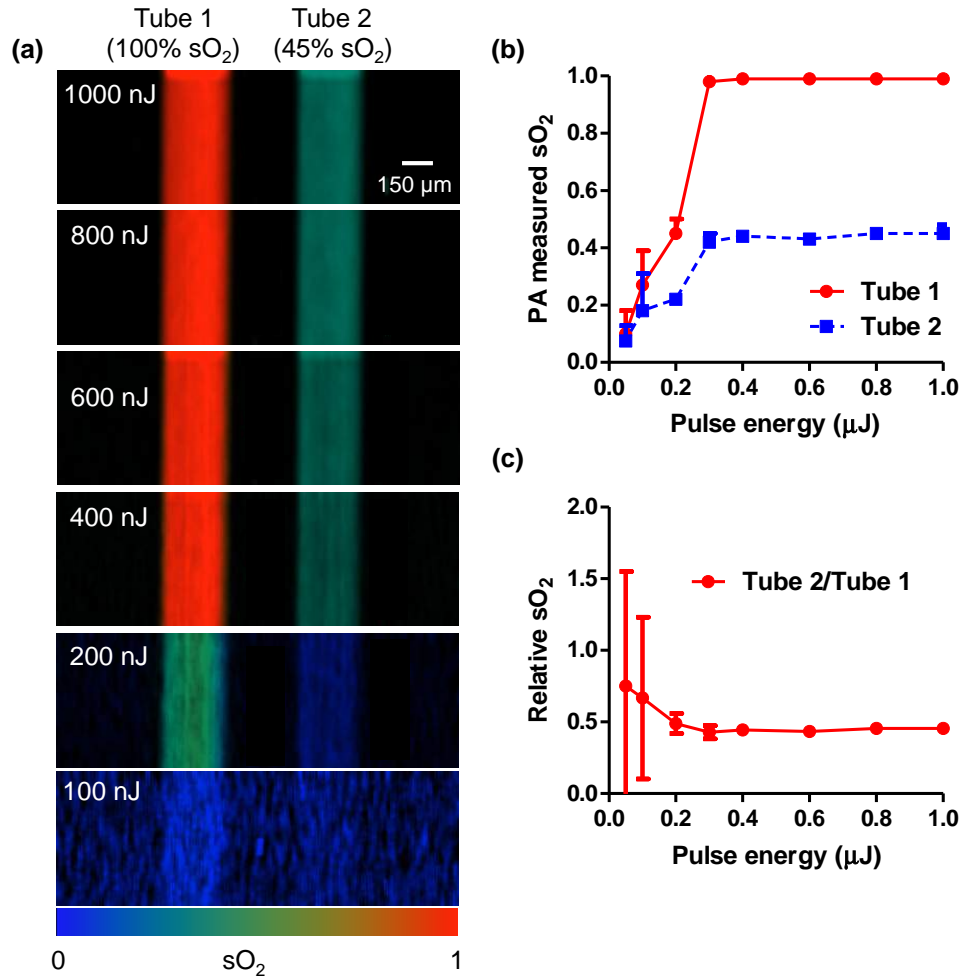
Supplementary Fig. 9. Pulse-width-based sO₂ measurement on blood phantoms, with different excitation pulse energies. (a) Two 300-µm-diameter tubes were filled with whole bovine blood. The light was focused at ~250 µm beneath the sample surface. The experiment conditions were the same as those in **Supplementary Fig. 3**. Tube 1 and Tube 2 had an average sO₂ of 100% and 45%, respectively, measured by the gas analyzer. The sO₂ values in the two tubes were then measured with PAM by using the pulse-width-based method, based on the calibrations in **Supplementary Fig. 3**. The excitation pulse energy was adjusted from 50 nJ to 1000 nJ. (b) The PAM measured sO₂ values averaged in each of the two tubes. The results show that the sO₂ measurement error was <3% with pulse energies ≥300 nJ. The sO₂ was underestimated by more than 50% when the pulse energy was reduced to ≤200 nJ. (c) The ratio of the sO₂ values between the two tubes. As the optical fluence was identical on the two tubes, the relative value was independent of the pulse energy as long as a sufficient saturation effect

was maintained. The results show that the relative sO_2 measurement error was <2% with pulse energies ≥300 nJ.

Supplementary Fig. 10. Pulse-width-based sO$_2$ measurement *in vivo*, with different excitation pulse energies. A 1×1 mm^2 area of a mouse ear, which contained an artery-vein pair, was imaged by PAM. The sO$_2$ in the artery-vein pair was measured by using the pulse-width-based method with excitation pulse energies from 50 nJ to 1000 nJ, based on the calibrations in **Supplementary Fig. 3**. The light was focused at ~250 μm beneath the tissue surface. The optical scattering above the artery-vein pair was negligible. The results show that the measured sO$_2$ values in the artery and vein with pulse energies ≥300 nJ were in the normal physiological range, while the measured sO$_2$ values in both the artery and vein with pulse energies ≤200 nJ were underestimated, similar to the results shown in **Supplementary Fig. 9**. The quantification of the sO$_2$ measurement *in vivo* is shown in **Fig. 1h**.
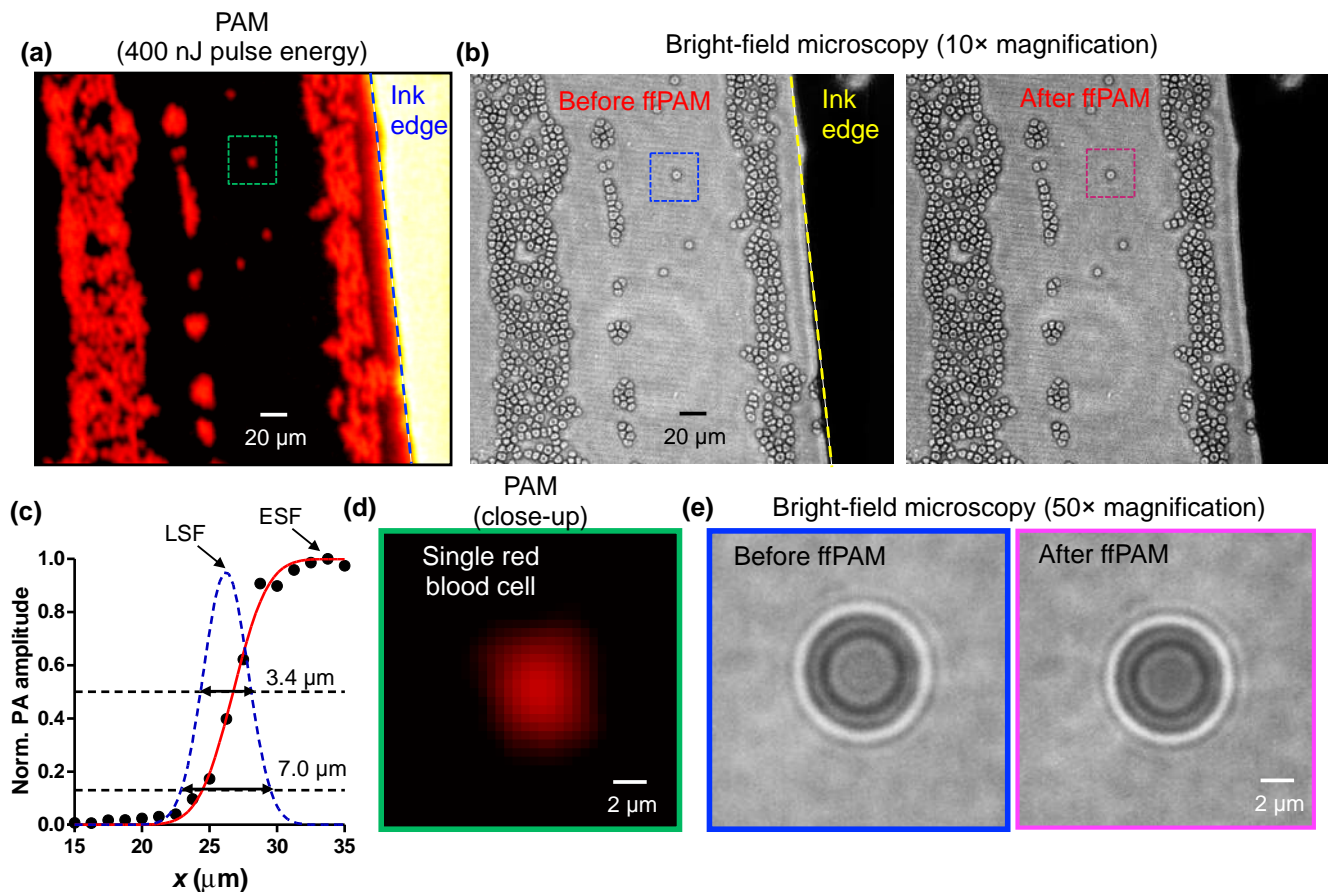
Supplementary Fig. 11. PAM and bright-field microscopy of a single layer of red blood cells (RBCs). (a) A single layer of freshly drawn mouse RBCs fixed on a glass slide was imaged by PAM (pulse energy: 400 nJ). Each picosecond laser pulse was followed by a nanosecond laser pulse with a time interval of 500 ns. The PAM image acquired with the picosecond excitation is shown here. The glass slide, protected by thin plastic film, was immersed in water. To measure the spatial resolution of PAM, a sharp black-ink edge on the glass slide was also imaged. (b) Bright-field microscopy (Zeiss AxioObserver) of the same region of RBCs as (a), conducted at 10× magnification before (left) and immediately after (right) the PAM imaging, showing the densely packed RBCs and their donut shapes after the PAM imaging. (c) Spatial resolution measurement of PAM. The edge spread function (ESF) (solid red line) of PAM was extracted by fitting the ink edge signals (solid black dots) with an error function. The line spread function (LSF) (dashed blue line) of PAM was then computed as the first derivative of the ESF. The lateral spatial resolution of PAM was measured as the full-width-at-half-maximum (FWHM) of

the LSF, ~3.4 µm. Note that the $1/e^2$ width of the LSF is ~7.0 µm. (d) A close-up PAM image of an individual RBC, as indicated by the dashed green box in (a). The donut shape of the RBC could not be resolved by PAM. (e) Bright-field microscopy of the same RBC as (d), at 50× magnification before (left) and immediately after (right) the PAM imaging, showing the cell's intact donut shape.
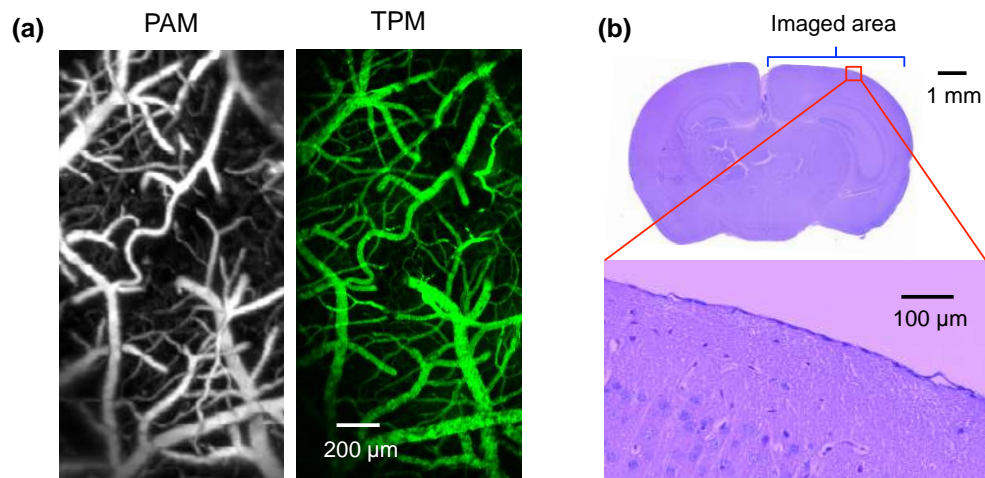
Supplementary Fig. 12. Two-photon microscopy and histological examination of a mouse brain imaged by PAM. (a) Two-photon microscopy (TPM) of cortical vasculature conducted after PAM imaging, showing no vessel leakage. FITC-dextran solution in PBS (150 µL, 2.5% w/v) was injected via a tail vein before the two-photon imaging. A 20× objective (NA = 0.70) was used to acquire high-resolution TPM images (excitation wavelength: 800 nm; emission filter wavelength: 495–540 nm). (b) Standard H&E histology of the mouse brain conducted after PAM imaging, showing no tissue damage. H&E stained brain sections were examined using bright-field microscopy (NanoZoomer, Hamamatsu) at 40× magnification.
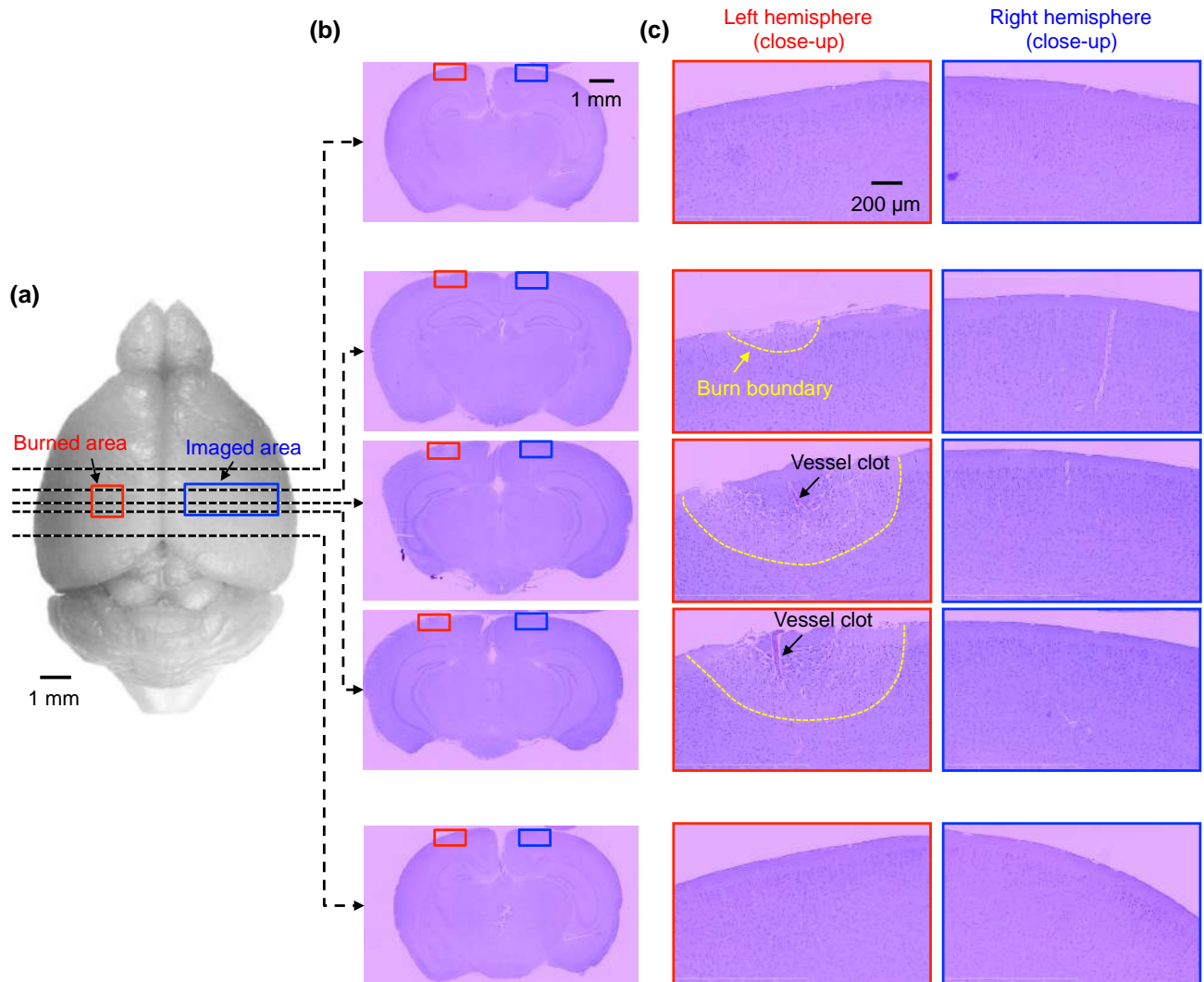
Supplementary Fig. 13. Histological examination with standard H&E staining of a mouse brain imaged by PAM. (a) A photograph of an extracted mouse brain after the blood was flushed. Before sacrificing the animal, the mouse's left hemisphere was illuminated by a continuous-wave laser (wavelength: 532 nm; power: 100 mW; spot size: 0.25 mm^2) for one minute to induce thermal coagulation (i.e., burn), as a positive control. The right hemisphere was repeatedly imaged by PAM for one minute with an excitation pulse energy of 1000 nJ and a volumetric frame rate of 1 Hz. The PAM focal plane was ~250 μm beneath the skull surface. After the PAM imaging, the mouse brain was extracted, fixed, sectioned and stained with standard H&E procedures. (b) Coronal slices of the mouse brain with H&E staining imaged under a bright-field optical microscope at 0.75× magnification. Five representative slices were

selected inside and outside the burned area and the imaged area, as indicated by the dashed lines in (a). (c) Close-up images of the burned area (left column, red boxes in (b)) and the PAM imaged area (right column, blue boxes in (b)) at 40× magnification. Clear burn boundaries and vessel clots were observed inside the burned area in the left hemisphere, while no damage was observed outside the burn area in the left hemisphere or inside the imaged area in the right hemisphere.
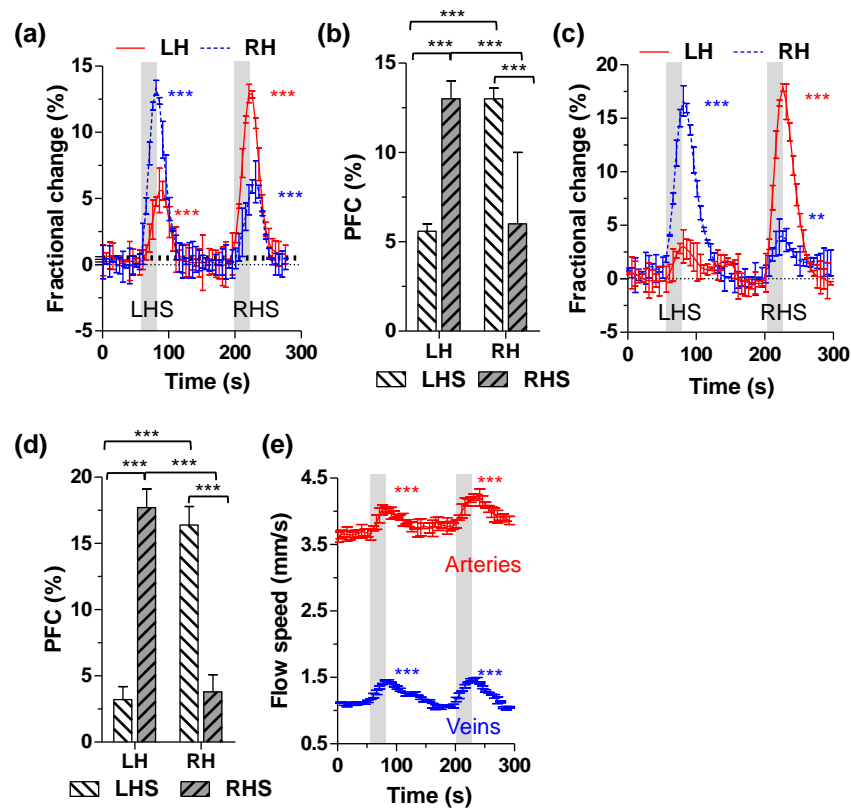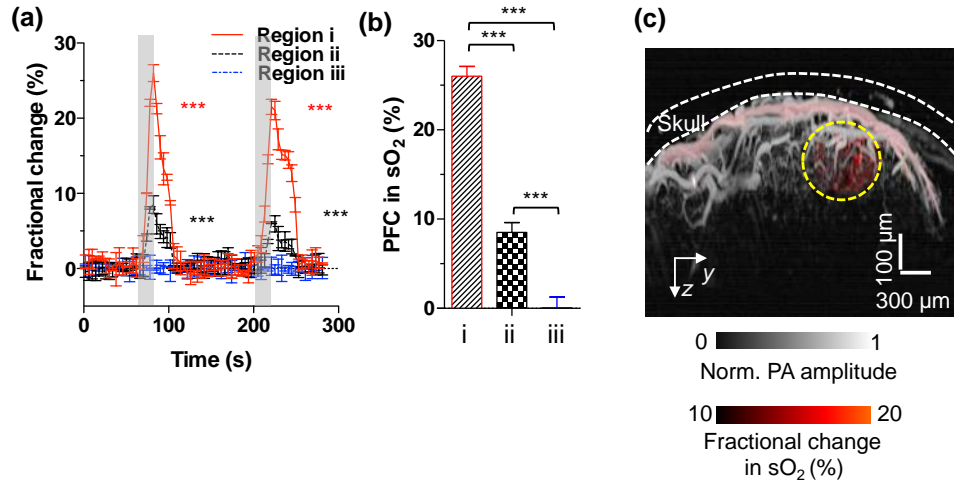
Supplementary Fig. 14. Quantification of mouse brain hemodynamic responses to electrical stimulations ($n = 6$). (a) Time courses of the spatially averaged fractional PA amplitude changes in the right hemisphere (RH) and left hemisphere (LH). The gray boxes outline the stimulation periods. LHS/RHS, left/right hindlimb stimulations. (b) Statistics of the peak fractional PA amplitude changes in the RH and LH. PFC, peak fractional change. (c) Time courses of the fractional arterial diameter changes in the RH and LH. (d) Statistics of the peak fractional changes in arterial diameters. (e) Time courses of the spatially averaged flow speeds in a selected artery-vein pair in the RH in response to the LHS. The data in (a)–(e) are averaged over five trials on each of the six mice, and the error bars denote standard errors. Statistics: paired student's t-test. P values: *** <0.001; **<0.05.
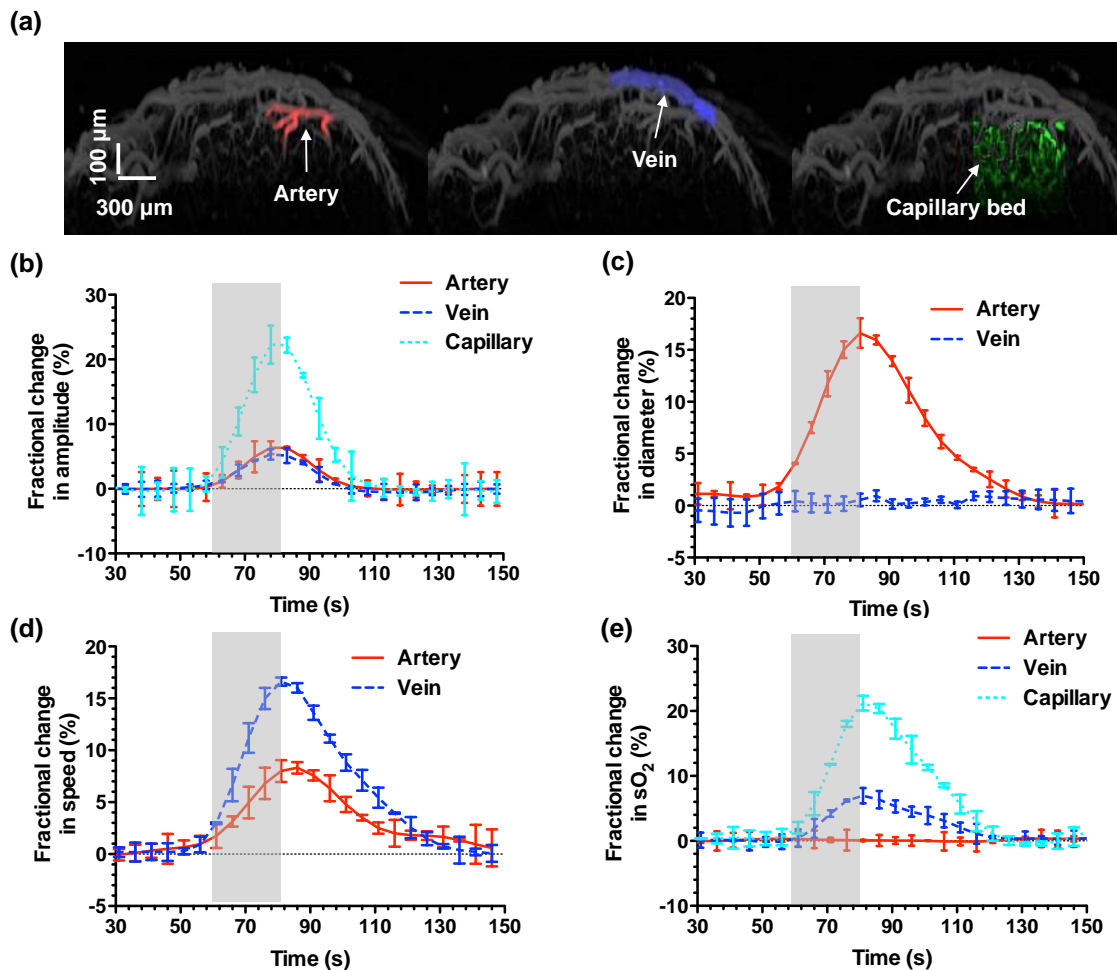
Supplementary Fig. 15. Quantification of vessel-type-based hemodynamic responses to electrical stimulations to hindlimbs. (a) Representative arteries, veins and capillary beds selected for quantification. (b) Time courses of the changes in total hemoglobin concentration in selected arteries, veins and deep capillary beds. (c) Time courses of the changes in vessel diameters in selected arteries and veins. The diameter changes in capillaries were unresolvable. (d) Time courses of the changes in blood flow speeds in selected arteries and veins. PAM could not resolve the flow speed changes in deep capillaries. (e) Time courses of the changes in sO_2 in selected arteries, veins and deep capillary beds.
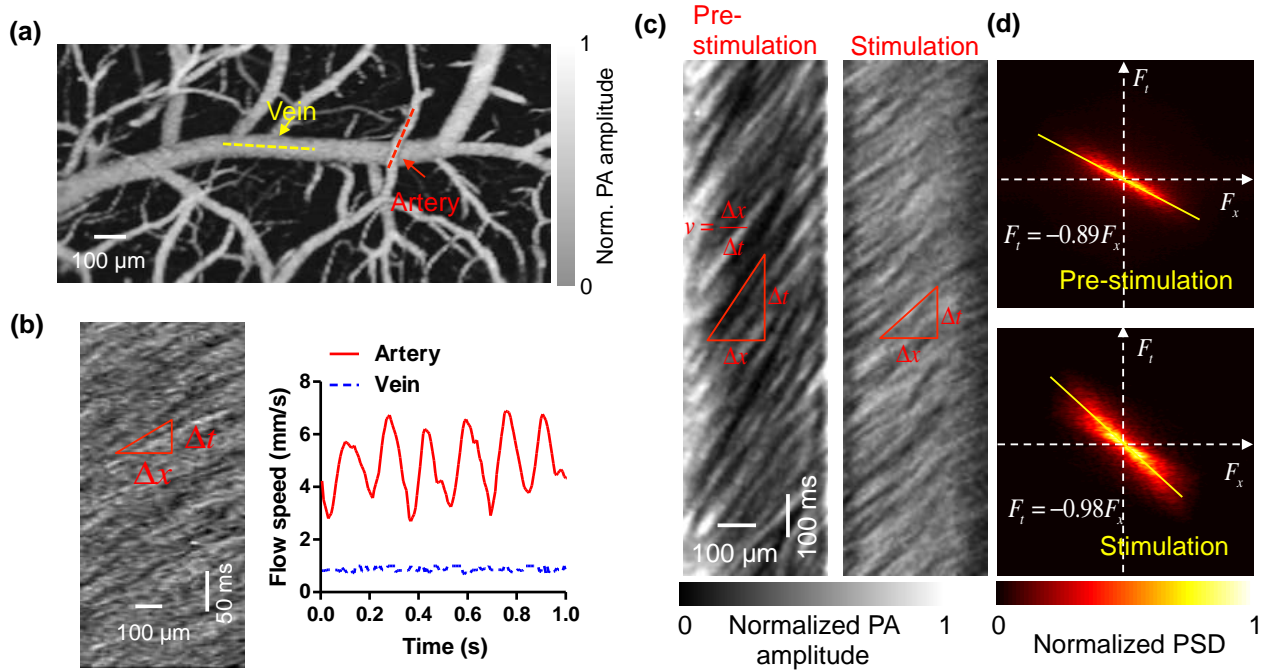
Supplementary Fig. 16. PAM of blood flow speed by fast line scanning. (a) PAM image of the somatosensory area in the right hemisphere. To measure the blood flow speed, fast line scanning (400 Hz) was performed along a vein and an artery, marked by the dashed lines, before and during the electrical stimulations to the left hindlimb. (b) Left panel: fast line scanning space–time plot acquired along the vein; Right panel: the time traces of the flow speeds in the artery and in the vein, showing the pulsations of arterial blood flow. (c) Fast line scanning space–time plots before (left panel) and during (right panel) electrical stimulations. The blood flow speeds were calculated from the slopes of the bright–dark streaks. (d) The flow speed can be estimated via a 2D Fourier transformation, where the slope between the temporal and spatial frequencies reflects the flow speed and direction. PSD, power spectral density.

Supplementary Fig. 17. Quantification of mouse brain oxygenation responses to electrical stimulations ($n = 6$). (a) Time courses of the spatially averaged fractional sO_2 changes in the three selected subregions shown in Figure 2c. The gray boxes outline the stimulation periods. (b) Statistics of the peak fractional sO_2 changes in the three subregions in response to the first stimulation. PFC, peak fractional change. (c) Depth-resolved sO_2 responses (shown in color) superimposed on the *y-z* projected vascular image (shown in gray). The core responding region is marked by the dashed circle. The data in (a)–(b) are averaged over five trials on each of the six mice, and the error bars denote standard errors. Statistics: paired student's *t*-test. *P* values: *** <0.001.

Supplementary video captions

Supplementary Video 1. Three-dimensional rendering of mouse cortical vasculature imaged by PAM with an intact skull.

Supplementary Video 2. Cross-sectional rendering of the mouse brain vasculature. Cross-sectional rendering of the mouse brain vasculature below a 0.6×0.6 mm^2 surface region, a composite image from 12 depth-scans of the optical focal zone. The shadows in deeper tissue were due to the blocking of light by superficial blood vessels. MAP, maximum amplitude projection.

Supplementary Video 3. PAM of cerebral responses to electrical stimulations to the hindlimbs. A 3×4 mm^2 cortical area covering the somatosensory regions of both hemispheres was imaged at a volumetric rate of 1 Hz. Fractional PA amplitude changes (shown in yellow), in response to the left hindlimb stimulation (LHS) and right hindlimb stimulation (RHS), were superimposed on the vascular image (shown in red). The curve at the bottom of the video shows the average PA signal amplitude in the somatosensory regions.

Supplementary Video 4. Volumetric rendering of oxygen saturation (sO$_2$). sO$_2$ was imaged below a 3×2 mm^2 surface region of a mouse brain at resting state. The sO$_2$ values were color-coded from blue (low oxygenation) to red (high oxygenation).

Supplementary Video 5. PAM of cerebral sO$_2$ responses to electrical stimulations to the left hindlimb. Left panel: sO$_2$ map of a 2×3 mm^2 cortical region covering the somatosensory region of the right hemisphere, acquired at a volumetric rate of 1 Hz. Right panel: close-up of the core responding region, marked by the dashed box in the left panel. The curve at the right bottom of the video shows the average sO$_2$ in the close-up region. Note that the resting-state frames acquired between 120 seconds and 200 seconds are omitted in the video.